Observation of non-Bloch parity-time symmetry and exceptional points

Peng Xue (✉ gnep.eux@gmail.com)

Beijing Computational Science Research Center   https://orcid.org/0000-0002-4272-2883

Lei Xiao

Beijing Computational Science Research Center

Tianshu Deng

Tsinghua University

Kunkun Wang

Beijing Computational Science Research Center

Zhong Wang

Tsinghua University   https://orcid.org/0000-0001-6254-6138

Wei Yi

University of Science and Technology of China   https://orcid.org/0000-0002-8880-6038

Observation of non-Bloch parity-time symmetry and exceptional points

Lei Xiao,[1] Tianshu Deng,[2] Kunkun Wang,[1] Zhong Wang,[2, *] Wei Yi,[3, 4, †] and Peng Xue[1, ‡]

[1] *Beijing Computational Science Research Center, Beijing 100084, China*
[2] *Institute for Advanced Study, Tsinghua University, Beijing, 100084, China*
[3] *CAS Key Laboratory of Quantum Information, University of Science and Technology of China, Hefei 230026, China*
[4] *CAS Center For Excellence in Quantum Information and Quantum Physics*

Parity-time (PT)-symmetric Hamiltonians have widespread significance in non-Hermitian physics. A PT-symmetric Hamiltonian can exhibit distinct phases with either real or complex eigen spectrum, while the transition points in between, the so-called exceptional points, give rise to a host of critical behaviors that holds great promise for applications. For spatially periodic non-Hermitian systems, PT symmetries are commonly characterized and observed in line with the Bloch band theory, with exceptional points dwelling in the Brillouin zone. Here, in non-unitary quantum walks of single photons, we uncover a novel family of exceptional points beyond this common wisdom. These "non-Bloch exceptional points" originate from the accumulation of bulk eigenstates near boundaries, known as the non-Hermitian skin effect, and inhabit a generalized Brillouin zone. Our finding opens the avenue toward a generalized PT-symmetry framework, and reveals the intriguing interplay among PT symmetry, non-Hermitian skin effect, and non-Hermitian topology.

While Hermiticity of Hamiltonians is a fundamental axiom in the standard quantum mechanics for closed systems, non-Hermitian Hamiltonians arise in open systems and possess unique features. Particularly, a wide range of non-Hermitian Hamiltonians, protected by the parity-time (PT) symmetry, can have entirely real eigenvalues [1–4]. A PT-symmetric Hamiltonian generally has two phases, the exact PT phase and the broken PT one, with real and complex eigenenergies, respectively. The transition points between these phases are called exceptional points, on which eigenvestates and eigenenergies coalesce while the Hamiltonian becomes nondiagonalizable. PT symmetry and exceptional points are ubiquitous in non-Hermitian systems, and lead to dramatic consequences and promising applications such as unidirectional invisibility [5], single-mode lasers [6, 7], enhanced sensing [8, 9], topological energy transfer [10], and non-reciprocal wave propagation [11, 12], to name just a few. In practice, physical systems with PT symmetry are often based on spatially periodic structures (e.g., photonic lattices or microwave arrays) [2, 13], where the notion of Bloch band greatly simplifies their characterization as each Bloch wave is treated independently.

Here we uncover a novel class of exceptional points beyond this Bloch-band picture. This work is partially stimulated by recent discoveries of non-Hermitian topological systems whose topological properties are highly sensitive to boundary conditions, in sharp contrast to their Hermitian counterparts. Specifically, for a generic family of non-Hermitian systems under the open-boundary condition (OBC), all eigenstates accumulate to the boundaries, whereas they always behave as extended Bloch waves under a periodic boundary condition (PBC). This phenomenon, known as the non-Hermitian skin effect, invalidates the conventional bulk-boundary correspondence and necessitates a re-definition of topological invariants [14–18]. Whereas topological physics has been the focus in previous studies [19–24], a fundamental question remains whether the non-Hermitian skin effect has significant consequences beyond topology, among which the interplay of non-Hermitian skin effect and PT symmetry is arguably the most intriguing [25, 26]. In this work, we experimentally observe exceptional points generated by the non-Hermitian skin effect. Despite a translationally invariant bulk, the observed exceptional points exist in a "generalized Brillouin zone" (GBZ) [19–21] (rather than the standard Brillioun zone), thus representing an unexplored class of exceptional points beyond the conventional Bloch-band framework. Just as the framework with conventional Bloch bands has been universally adopted to describe periodic lattices in physical systems ranging from condensed matter to photonics, the generalized mechanism of PT symmetry, confirmed by our observation of "non-Bloch exceptional points", is universally relevant to non-Hermitian platforms.

In general, a discrete-time, non-unitary quantum walk can be characterized by $|\psi(t)\rangle = U^t |\psi(0)\rangle$ ($t = 0, 1, 2, \cdots$), which amounts to a stroboscopic simulation of the time evolution with initial state $|\psi(0)\rangle$, and generated by the non-Hermitian effective Hamiltonian H_{eff} with $U := e^{-iH_{\text{eff}}}$. To be concrete, we take the following one-dimensional Floquet operator

$$U = R\left(\frac{\theta_1}{2}\right) S_2 R\left(\frac{\theta_2}{2}\right) M R\left(\frac{\theta_2}{2}\right) S_1 R\left(\frac{\theta_1}{2}\right), \quad (1)$$

where the shift operators, $S_1 = \sum_x |x\rangle\langle x| \otimes |0\rangle\langle 0| + |x+1\rangle\langle x| \otimes |1\rangle\langle 1|$ and $S_2 = \sum_x |x-1\rangle\langle x| \otimes |0\rangle\langle 0| + |x\rangle\langle x| \otimes |1\rangle\langle 1|$, selectively shift the walker along a one-dimensional lattice (with lattice sites labelled by x) in a direction that
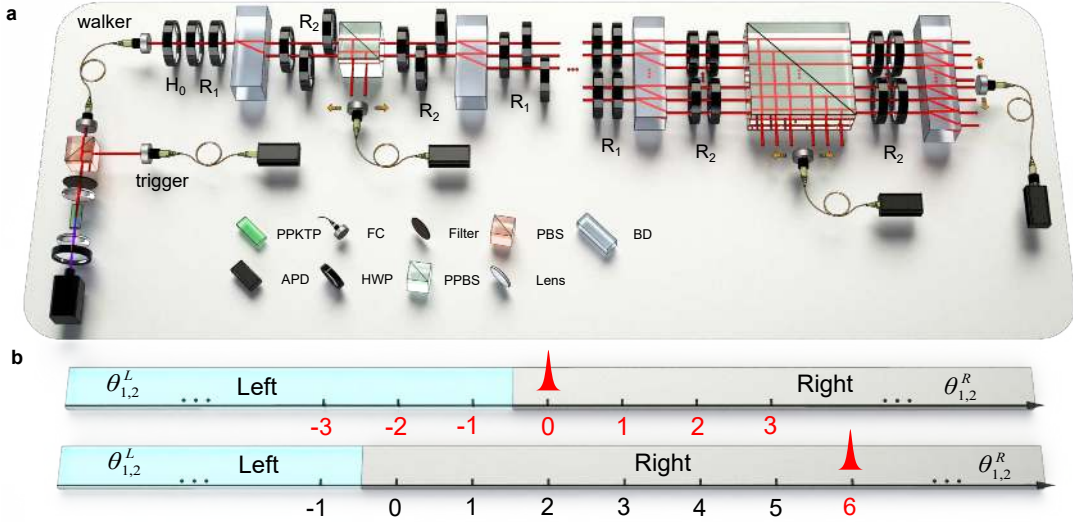
FIG. 1. **Experimental implementation. a**, A pair of photons is generated via the spontaneous parametric down conversion in the periodically poled potassium titanyl phosphate crystal (PPKTP), with one serving as a trigger and the other (walker) projected into the quantum-walk network as the walker photon. After passing through a polarizing beam splitter (PBS) and a half-wave plate (HWP), the polarization of the walker photon is initialized as $|0\rangle$. It then undergoes a quantum walk through an interferometric network, composed of HWPs, beam displacers (BDs), and partially polarizing beam splitter (PPBS), and is finally detected by avalanche photodiodes (APDs), in coincidence with the trigger photon. **b**, The domain-wall geometry of non-Hermitian quantum walks. Upper panel (Scheme I): the walker starts near the domain wall at $x = 0$. Lower panel (Scheme II): the walker starts from the bulk (i.e., far away from the domain wall) position $x = 6$.
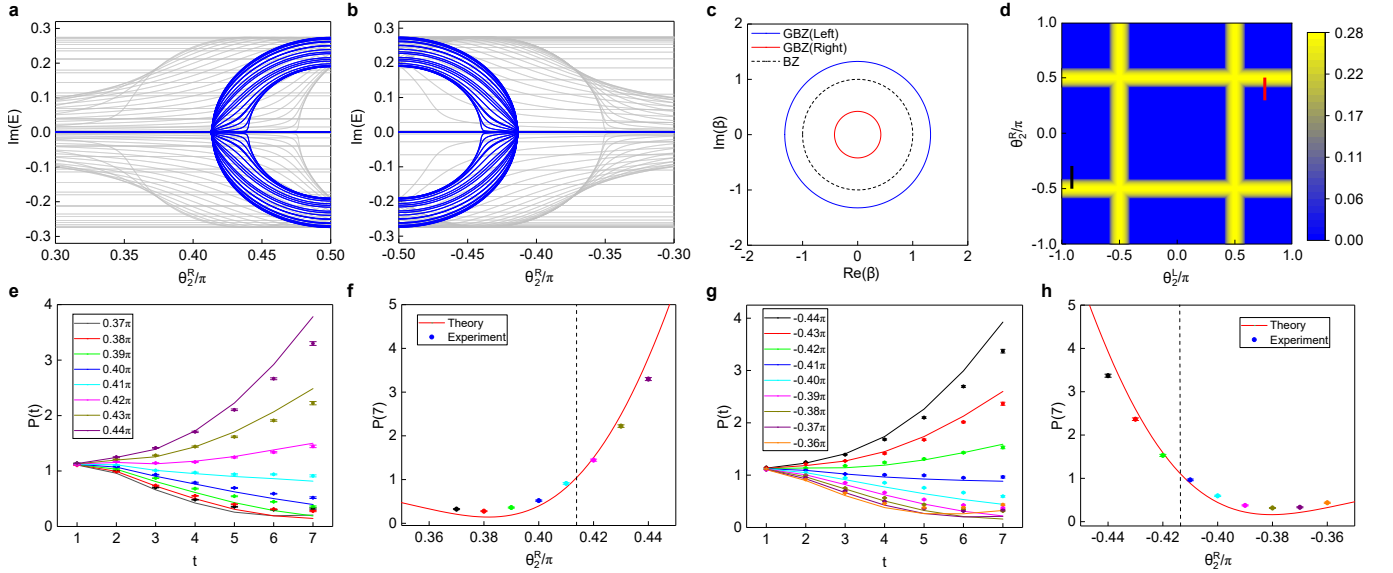

FIG. 2. **Non-Bloch exceptional points from domain-wall measurements. a, b**, Imaginary part of quasienergies, $\text{Im}(E)$ versus θ_2^R. Other coin parameters are fixed at $\theta_1^R = 0.5625\pi$ and $\theta_1^L = -0.0625\pi$. We take $\theta_2^L = 0.75\pi$ and -0.9735π for **a** and **b**, respectively. Blue and gray lines represent the OBC (non-Bloch) and PBC (Bloch) spectra, respectively. The blue non-Bloch spectra feature an exceptional point at $|\theta_2^R| = 0.413\pi$, while the gray Bloch spectra remain complex-valued throughout. **c**, Brillouin zone and GBZ for $\theta_1^R = 0.5625\pi$, $\theta_1^L = -0.0625\pi$, $\theta_2^R = -0.44\pi$ and $\theta_2^L = -0.9375\pi$. **d**, Numerically calculated $\max[\text{Im}(E)]$ for $\theta_1^R = 0.5625\pi$ and $\theta_1^L = -0.0625\pi$. The yellow (blue) region is the broken (exact) PT phase. The red and black cuts correspond to **a, e, f** and **b, g, h**, respectively. **e**, Experimentally measured $P(t)$ (symbols) with an initial state $|\psi(t=0)\rangle = |0\rangle_x \otimes |0\rangle_{\text{coin}}$ up to seven steps for eight different values of θ_2^R, together with the theoretical predictions (curves). Other coin parameters are the same as in **a**, e.g., $\theta_2^L = 0.75\pi$. **f**, $P(t=7)$ under the same parameters as those in **c**. Error bars indicate the statistical uncertainty obtained by assuming Poissonian statistics. **g, h**, The same as **e, f** except that $\theta_2^L = -0.9735\pi$. The loss parameter is fixed at $\gamma = 0.2746$ throughout our experiment.

depends on its internal coin state $|0\rangle(|1\rangle)$, the $+1$ (-1) eigenstate of the Pauli matrix σ_z. The coin operator $R(\theta) = \mathbb{1}_{\mathrm{w}} \otimes e^{-i\theta\sigma_y}$, with $\mathbb{1}_{\mathrm{w}} = \sum_x |x\rangle\langle x|$, rotates coin states without shifting the walker position. The gain and loss is implemented by $M = \mathbb{1}_{\mathrm{w}} \otimes e^{\gamma\sigma_z}$.

We implement the quantum walk using a single-photon interferometric network [Fig. 1a], where coin states $|0\rangle$ and $|1\rangle$ are encoded in the horizontal and vertical photon polarizations, respectively. Rotations of the coin states (R) are implemented by half-wave plates (HWPs). Shift operators $S_{1,2}$ are realized by beam displacers (BDs) that allow the transmission of vertically polarized photons while displacing horizontally polarized ones into neighboring positions. Finally, the gain/loss is implemented by a partially polarizing beam splitter (PPBS), which reflects state $|1\rangle$ with a probability p, and directly transmits state $|0\rangle$. Thus, the PPBS realizes $M_E = \mathbb{1}_{\mathrm{w}} \otimes \left(|0\rangle\langle 0| + \sqrt{1-p}|1\rangle\langle 1|\right)$, which is related to M as $M = e^{\gamma}M_E$, with $\gamma = -\frac{1}{4}\ln(1-p)$. We therefore readout $|\psi(t)\rangle$ from our experiment with M_E by adding a factor $e^{\gamma t}$. More details of our experimental setup can be found in Methods.

Under the Floquet operator U, the directional hopping in $S_{1,2}$ and the gain/loss in M conspire to generate non-Hermitian skin effect [14]. When a domain wall is created between two regions with different parameters, e.g., $\theta_{1,2}^L$ and $\theta_{1,2}^R$ for the left and right regions in Fig. 1b, all the eigenstates of U are localized at the domain wall [14]. While the non-Hermitian skin effect dramatically affects topological properties, here we focus on the impact of non-Hermitian skin effect on the emergence of PT symmetry and exceptional points.

The exact (broken) PT phase corresponds to the absence (presence) of nonzero imaginary parts in the eigen spectrum (quasienergies) of H_{eff}. In Figs. 2a, b, we show in blue the calculated imaginary parts of quasienergies, $\mathrm{Im}(E)$, for the domain-wall geometry with OBC at the two ends [see Fig. 1b]. For both Figs. 2a, b, an exceptional point is found as θ_2^R is varied while fixing other parameters. Remarkably, the exceptional point cannot be deduced from the Bloch band theory. The Bloch theory suggests that the continuous bulk spectra of U under the domain-wall geometry are the union of the spectra corresponding to the left and right bulks, which are respectively obtained from the Bloch Floquet operator $U(k)$ $(k \in [0, 2\pi]$, i.e., within the standard Brillioun zone) associated with the left (with parameters $\theta_{1,2}^L$) and right (with $\theta_{1,2}^R$) bulk. These spectra are shown in gray in Figs. 2a, b, which dramatically differ from the actual (non-Bloch) spectra under the domain-wall geometry.

This discrepancy is due to the aforementioned non-Hermitian skin effect. The exponential decay of eigenstates in the real space means that the Bloch phase factor e^{ik}, which corresponds to extended plane waves, should be replaced by a factor β $(|\beta| \neq 1$ in general) in order to generate the eigen spectra under the OBC. Furthermore, β must belong to a closed loop in the complex plane, dubbed the GBZ [19, 21], which typically deviates from

the unit circle [Fig. 2c]. For $\beta \in$ GBZ, eigenenergies under the OBC are recovered by performing the analytic continuation $U(k)|_{e^{ik}\rightarrow\beta}$, and taking the logarithm of eigenvalues of $U(\beta)$. Crucially, we find that $U(\beta)$ satisfies the η-pseudo-unitarity

$$\eta U^{-1}(\beta)\eta^{-1} = U^{\dagger}(\beta)\big|_{\beta\in\mathrm{GBZ}}, \tag{2}$$

when $|\cos\theta_2^{L(R)}| > |\tanh\gamma|$ (see Methods). Here $\eta = \sum_n |\chi_n\rangle\langle\chi_n|$, where $\{|\chi_n\rangle\}$ is the collection of left eigenstates of $U(\beta)$. Equation (2) corresponds to the η-pseudo-Hermiticity of the non-Hermitian effective Hamiltonian: $\eta H_{\mathrm{eff}}(\beta)\eta^{-1} = H_{\mathrm{eff}}^{\dagger}(\beta)$ [27, 28], which is a generalization of the PT symmetry, and guarantees the reality of quasienergies as long as the relation holds. As such, the GBZ theory predicts non-Bloch exceptional points at

$$|\cos\theta_2^{L(R)}| = |\tanh\gamma|. \tag{3}$$

We observe exceptional points by probing probabilities of the photon surviving in the quantum walk after each time step t, which are constructed from photon-number measurements up to t (see Methods for details). They are then multiplied by a factor $e^{2\gamma t}$ (due to the aforementioned difference between M_E and M) to yield the corrected probability $P(t)$ that corresponds to the wavefunction norm, whose long-time behavior is $P(t) = \langle\psi(t)|\psi(t)\rangle \sim e^{2\max[\mathrm{Im}(E)]t}$. Therefore, an exponential growth of $P(t)$ indicates the broken PT phase, which enables us to extract the location of exceptional points by tracking the time evolution of the corrected probability. Experimentally, this is achieved through two schemes: (I) the domain wall scheme and (II) the bulk scheme.

In the first scheme, we initiate the photon walker near the domain wall, as illustrated in the upper panel of Fig. 1b, with the initial state $|\psi(t=0)\rangle = |0\rangle_x \otimes |0\rangle_{\mathrm{coin}}$. We then measure the corrected probability along the red and black cuts in the numerically simulated phase diagram [Fig. 2d], where the blue and yellow regions correspond to the exact and broken PT phase, respectively. In Fig. 2e (red cut), $P(t)$ grows with t for $\theta_2^R \geq 0.42\pi$ and decreases for $\theta_2^R \leq 0.41\pi$. Therefore, we infer the presence of an exceptional point between $\theta_2^R = 0.41\pi$ and 0.42π. This is consistent with Eq. (3), which predicts an exceptional point at $\theta_2^R = \pm 0.413\pi$. We arrive at the same conclusion by measuring corrected probabilities at the time step $t = 7$ [Fig. 2f], which become prominently larger than 1 in the broken PT phase. Similarly, Figs. 2g, h (blue cut) indicate an exceptional point in the region $\theta_2^R \in [-0.42\pi, -0.41\pi]$, again consistent with Eq. (3).

The second scheme is based on *in situ* measurements in the bulk. The walker starts from a position $x = x_0$ far from the domain wall [Fig. 1b, lower panel], and the subsequent corrected probability at $x = x_0$, i.e., $P_{x_0}(t) = |\langle 0| \otimes \langle x_0|\psi(t)\rangle|^2 + |\langle 1| \otimes \langle x_0|\psi(t)\rangle|^2$, is measured. In the broken PT phase, the corrected probability grows as $P_{x_0}(t) \propto e^{\alpha t}$, where α is given by the imaginary part of quasienergies at certain special points of
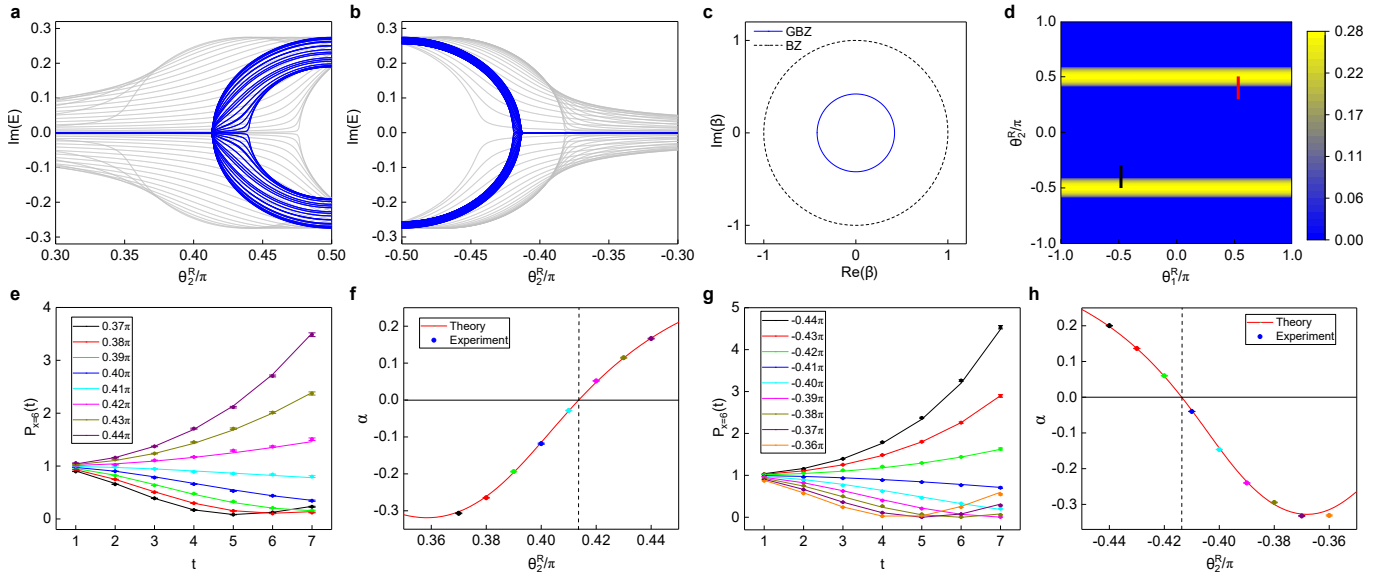
FIG. 3. **Non-Bloch exceptional points from bulk measurements.** **a**, $\mathrm{Im}(E)$ versus θ_2^R, with $\theta_1^R = 0.5625\pi$ fixed. **b**, $\mathrm{Im}(E)$ versus θ_2^R, with $\theta_1^R = -0.4688\pi$ fixed. **c**, GBZ of the right region, for $\theta_1^R = -0.4688\pi$ and $\theta_2^R = -0.44\pi$. **d**, Numerically calculated $\max[\mathrm{Im}(E)]$. The blue and yellow regions correspond to the exact and broken PT phase, respectively. **e**, Experimentally measured $P_{x=6}(t)$ (symbols) with an initial state $|\psi(0)\rangle = |6\rangle_x \otimes |0\rangle_{\text{coin}}$ for eight values of θ_2^R, compared to the theoretical predictions (curves). Here we fix $\theta_1^R = 0.5625\pi$. **f**, Exponent α versus θ_2^R extracted from the data in **e**. The red line is plotted from numerical simulations of 7-step evolutions. **g**, **h** The same as **c**, **d**, except that $\theta_2^R = -0.5\pi$. **e**, **f** and **g**, **h** correspond to the red and black cuts in the phase diagram **d**, respectively. The left region is idle throughout measurements, which are performed in the right region only. Without loss of generality, we take $\theta_1^L = -0.0625\pi$ and $\theta_2^L = 0.75\pi$ for **a**, **b**, and $\theta_1^L = -0.0625\pi$ and $\theta_2^L = -0.9375\pi$ for **g**, **h**.

the GBZ [25, 26]. In our experiment, we fix $x_0 = 6$ in the right region, leaving the left region idle. The imaginary parts of quasienergy spectra under OBC are plotted in Figs. 3a, b, along the red and black cuts in Fig. 3d, respectively. The spectra are calculated by diagonalizing $U(\beta)|_{\beta \in \text{GBZ}}$ for the right region, with GBZ shown in Fig. 3c. Along the red cut ($\theta_1^R = 0.5625\pi$), the measured $P_{x=6}(t)$ exhibits growth for $\theta_2^R \geq 0.42\pi$, and decreases for $\theta_2^R \leq 0.42\pi$ as illustrated in Fig. 3e, indicating an exceptional point within $[0.41\pi, 0.42\pi]$. This is consistent with Fig. 3a. Moreover, we fit $P_{x=6}(t)$ exponentially in Fig. 3f. While the accuracy in α is limited by the small number of experimentally feasible steps (see Methods for further discussions), the fitted α does yield qualitatively consistent results: The sign of α is positive (negative) in the broken (exact) PT phase. A similar exceptional point is observed along the black cut ($\theta_1^R = -0.9375\pi$) in Figs. 3g, h.

The significance of the observed non-Bloch PT symmetry and exceptional points is further enhanced by the following deep understanding: In the presence of non-Hermitian skin effect, the Bloch energy spectra (calculated from the Brillouin zone) can never have PT symmetry. In fact, recent theoretical works prove that, if a sys-

tem features non-Hermitian skin effect under the OBC, the associated Bloch spectra (calculated from the Brillouin zone) must form loops in the complex plane [29, 30]. However, loop-like spectra cannot lie in the real axis, thus forbidding entirely real spectrum. In sharp contrast, the non-Bloch spectra calculated from the GBZ, which correctly reflect eigenenergies under the experimentally relevant OBC, form arcs instead of loops. Real spectra and PT symmetry are henceforth enabled. Therefore, non-Bloch PT symmetry is the only general mechanism for achieving PT symmetry in the presence of non-Hermitian skin effect.

The observed interplay between non-Hermitian skin effect and PT symmetry underlines a fundamentally new mechanism for PT symmetry and exceptional points. Since both the non-Hermitian skin effect and PT symmetry are generic features of a large class of non-Hermitian systems, the mechanism is general and applies to a variety of non-Hermitian platforms ranging from photonic lattices to cold atoms. In view of the potential utilities of exceptional points, the non-Bloch exceptional points observed here would inspire novel designs and applications such as high-quality single-mode lasers and enhanced sensing with high spatial resolutions [6–9, 17].

[1] Bender C. M. & Boettcher S. Real spectra in non-Hermitian Hamiltonians having PT symmetry. *Phys.* *Rev. Lett.* **80**, 5243-5246 (1998).

[2] El-Ganainy R. *et al.* Non-Hermitian physics and PT symmetry. *Nat. Phys.* **14**, 11-19 (2018).

[3] Özdemir Ş. K. *et al.* Parity-time symmetry and exceptional points in photonics. *Nat. Mater.* **18**, 783-798 (2019).

[4] Miri M. A. & Alù A. Exceptional points in optics and photonics. *Science* **363**, eaar7709 (2019).

[5] Regensburger A. *et al.* Parity-time synthetic photonic lattices. *Nature* **488**, 167-171 (2012).

[6] Feng L., Wong Z. J., Ma R. M., Wang Y. & Zhang X. Single-mode laser by parity-time symmetry breaking. *Science* **346**, 972-975 (2014).

[7] Hodaei H., Miri M. A., Heinrich M., Christodoulides D. N. & Khajavikhan M. Parity-time-symmetric microring lasers. *Science* **346**, 975-978 (2014).

[8] Chen W., Özdemir Ş. K., Zhao G., Wiersig J. & Yang L. Exceptional points enhance sensing in an optical microcavity. *Nature* **548**, 192-196 (2017).

[9] Hodaei H. *et al.* Enhanced sensitivity at higher-order exceptional points. *Nature* **548**, 187-191 (2017).

[10] Xu H., Mason D., Jiang L. & Harris J. G. E. Topological energy transfer in an optomechanical system with exceptional points. *Nature* **537**, 80-83 (2016).

[11] Christian E. R. *et al.* Observation of parity-time symmetry in optics. *Nat. Phys.* **6**, 192-195 (2010).

[12] Peng B. *et al.* Parity-time-symmetric whispering-gallery microcavities. *Nat. Phys.* **10**, 394-398 (2014).

[13] Makris K. G., El-Ganainy R., Christodoulides D. N. & Musslimani Z. H. Beam dynamics in PT symmetric optical lattices. *Phys. Rev. Lett.* **100**, 103904 (2008).

[14] Xiao L. *et al.* Non-Hermitian bulk-boundary correspondence in quantum dynamics. *Nat. Phys.* **16**, 761-766 (2020).

[15] Helbig T. *et al.* Generalized bulk-boundary correspondence in non-Hermitian topolectrical circuits. *Nat. Phys.* **16**, 747-750 (2020).

[16] Ghatak A., Brandenbourger M., van Wezel J. & Coulais C. Observation of non-Hermitian topology and its bulk-edge correspondence. *arXiv:1907.11619.*

[17] Weidemann S. *et al.* Topological funneling of light. *Science* **368**, 311-314 (2020).

[18] Hofmann T. *et al.* Reciprocal skin effect and its realization in a topolectrical circuit. *Phys. Rev. Research* **2**, 023265 (2020).

[19] Yao S. & Wang Z. Edge states and topological invariants of non-Hermitian systems. *Phys. Rev. Lett.* **121**, 086803 (2018).

[20] Yao S., Song F. & Wang Z. Non-Hermitian chern bands. *Phys. Rev. Lett.* **121**, 136802 (2018).

[21] Yokomizo K. & Murakami S. Non-Bloch band theory of non-Hermitian systems. *Phys. Rev. Lett.* **123**, 066404 (2019).

[22] Kunst F. K., Edvardsson E., Budich J. C. & Bergholtz E. J. Biorthogonal bulk-boundary correspondence in non-Hermitian systems. *Phys. Rev. Lett.* **121**, 026808 (2018).

[23] Lee C. H. & Thomale R. Anatomy of skin modes and topology in non-Hermitian systems. *Phys. Rev. B* **99**, 201103(R) (2019).

[24] Kawabata K., Shiozaki K., Ueda M. & Sato M. Symmetry and topology in non-Hermitian physics. *Phys. Rev. X* **9**, 041015 (2019).

[25] Longhi S. Probing non-Hermitian skin effect and non-Bloch phase transitions. *Phys. Rev. Research* **1**, 023013 (2019).

[26] Longhi S. Non-Bloch PT symmetry breaking in non-Hermitian photonic quantum walks. *Opt. Lett.* **44**, 5804-5807 (2019).

[27] Mostafazadeh A. Pseudo-Hermiticity versus PT symmetry. *J. Math. Phys.* **43**, 205-214 (2002).

[28] Mostafazadeh A. Pseudo-Hermiticity versus PT symmetry. II. *J. Math. Phys.* **43**, 2814-2816 (2002).

[29] Okuma N., Kawabata K., Shiozaki K. & Shiozaki M. Topological origin of non-Hermitian skin effects. *Phys. Rev. Lett.* **124**, 086801 (2020).

[30] Shiozaki K., Yang Z. & Fang C. Correspondence between winding numbers and skin modes in non-Hermitian systems. *arXiv:1910.01131.*

METHODS

Experimental Methods

As illustrated in Fig. 1a and discussed in the main text, coin states are encoded in the photon polarizations, with $|0\rangle$ and $|1\rangle$ corresponding to the horizontal and vertical polarizations, respectively. The walker states are represented by the spatial modes of photons, with the lattice sites labelled by x. The walker photon is initialized at either the domain wall ($x = 0$) or at a site far from the domain wall ($x = x_0$), and is projected onto one of the polarization states $|0\rangle$ by a polarizing beam splitter (PBS) and a half-wave plate (HWP). While the coin operator R is implemented by HWPs, the shift operator S_1 (S_2) is realized by a beam displacer (BD), which allows the direct transmission of vertically polarized photons and displaces horizontally polarized photons laterally to a neighboring spatial mode.

Non-unitarity is introduced by photon loss, which is realized by a mode-selective loss operator

$$M_E = \mathbb{1}_{\mathrm{w}} \otimes \left(|0\rangle\langle 0| + \sqrt{1-p}|1\rangle\langle 1| \right) \tag{4}$$

with $\mathbb{1}_{\mathrm{w}} = \sum_x |x\rangle\langle x|$, realizing a partial measurement at every time step. The loss operator M_E is implemented by a partially polarizing beam splitter (PPBS). In our experiment, M_E, rather than $M = e^{\gamma} M_E$ [$\gamma = -\frac{1}{4}\ln(1-p)$], is implemented. Nevertheless, the experimentally implemented t-step quantum-walk dynamics can be mapped to that under U by multiplying a time-dependent factor $e^{\gamma t}$. Under the Floquet operator U, the time-evolved state is given by $|\psi(t)\rangle = U^t|\psi(0)\rangle$ ($t = 0, 1, 2, \cdots$). Therefore, a quantum walk stroboscopically simulates the non-unitary time evolution generated by the non-Hermitian effective Hamiltonian H_{eff}, where $U := e^{-iH_{\mathrm{eff}}}$. Typical eigen spectra of H_{eff} are shown in Figs. 2b and 3b.

In the first scheme of detecting non-Bloch exceptional points, the walker starts from $x = 0$ shown in Fig. 1b. We measure the corrected probability after t-step quantum-walk dynamics $P(t) = \langle\psi(t)|\psi(t)\rangle$ with initial state $|\psi(0)\rangle = |0\rangle \otimes |0\rangle$ through photon-number measurements, which are registered by the coincidences between one of the avalanche photodiodes (APDs) in the detection stage and that for the trigger photon. The corrected probability $P(t)$ can be calculated from the photon-number measurements multiplied (i.e., corrected) by a time-dependent factor $e^{2\gamma t}$

$$P(t) = e^{2\gamma t} \sum_x \frac{N(t,x)}{\sum_x \left[N(t,x) + \sum_{t'=1}^{t} N_L(t',x) \right]}, \tag{5}$$

where $N(t,x)$ is the number of the photons detected at x after a t-step evolution and $N_L(t,x)$ is the photon loss caused by the partial measurement M_E at the time step t.

For the second scheme in which the walker starts from $x = x_0$ far from the domain wall, we measure the corrected probability at $x = x_0$ after a t-step quantum walk $P_{x_0}(t) = \left| \langle 0| \otimes \langle x_0|\psi(t)\rangle \right|^2 + \left| \langle 1| \otimes \langle x_0|\psi(t)\rangle \right|^2$, with initial state $|\psi(0)\rangle = |x_0\rangle \otimes |0\rangle$. The expression for $P_{x_0}(t)$ is therefore

$$P_{x_0}(t) = e^{2\gamma t} \frac{N(t,x_0)}{\sum_x \left[N(t,x) + \sum_{t'=1}^{t} N_L(t',x) \right]}. \tag{6}$$

If all the eigenenergies of the system are real, i.e., the system is in the exact parity-time (PT) phase, $P(t)$ approaches a steady-state value at long times, while $P_{x_0}(t)$ decays towards 0 by a power law [25]. In contrast, after the system crosses the exceptional point and becomes PT broken, quasienergies are typically complex. $P_{x_0}(t)$ and $P(t)$ would then increase exponentially with time.

To demonstrate the exponential dependence of $P_{x_0}(t)$ in time (for the PT broken phase), we numerically fit $P_{x_0}(t)$ for quantum-walk dynamics up to $t = 150$ steps, with either exponential or power-law dependence in time. We show the accumulated variance $\sum_t [P_{x=6}(t) - f(t)]^2/f^2(t)$ in Extended Data Fig. 1 across the exceptional points, where $f(t)$ is the fitting function. Apparently, the errors with the exponential fit is always smaller in the PT broken phase, and larger in the exact PT phase. This justifies the exponential fit in Fig. 3 of the main text.

Generalized Brillouin zone, non-Bloch PT symmetry, and non-Bloch exceptional points

In this section, we first derive the generalized Brillouin zone (GBZ). The analytic continuation of the Bloch Hamiltonian (or Floquet operator) to the GBZ yields the actual quasienergy spectra for the experimentally relevant open-boundary systems. We then show the non-Bloch PT symmetry, i.e., PT symmetry and exceptional points that exist

in the GBZ rather than the conventional Brillouin zone (BZ). We will derive the analytic formula for the non-Bloch exceptional points given in the main article: $|\cos \theta_2| = |\tanh \gamma|$.

Generalized Brillouin zone. We start from the Floquet operator U, which can be decomposed as $U = FMG$, where

$$F = R\left(\frac{\theta_1}{2}\right) S_2 R\left(\frac{\theta_2}{2}\right), \tag{7}$$

$$G = R\left(\frac{\theta_2}{2}\right) S_1 R\left(\frac{\theta_1}{2}\right), \tag{8}$$

$$M = \mathbb{1}_{\mathrm{w}} \otimes e^{\gamma \sigma_z}. \tag{9}$$

Here, the coin operator R and the shift operator $S_{1,2}$ read

$$R(\theta) = \mathbb{1}_{\mathrm{w}} \otimes R_c(\theta), \tag{10}$$

$$S_1 = \sum_x |x\rangle\langle x| \otimes |0\rangle\langle 0| + |x+1\rangle\langle x| \otimes |1\rangle\langle 1|, \tag{11}$$

$$S_2 = \sum_x |x-1\rangle\langle x| \otimes |0\rangle\langle 0| + |x\rangle\langle x| \otimes |1\rangle\langle 1|, \tag{12}$$

with $\mathbb{1}_{\mathrm{w}} = \sum_x |x\rangle\langle x|$ and $R_c(\theta) = e^{-i\theta \sigma_y}$. Since $\theta_1(x)$ and $\theta_2(x)$ are both constants in the bulk (i.e., away from the domain wall), we rewrite the Floquet operator as

$$U = \sum_x |x\rangle\langle x+1| \otimes A_m + |x\rangle\langle x-1| \otimes A_p + |x\rangle\langle x| \otimes A_s, \tag{13}$$

where

$$A_m = R_c\left(\frac{\theta_1}{2}\right) P_0 R_c\left(\frac{\theta_2}{2}\right) M_c R_c\left(\frac{\theta_2}{2}\right) P_0 R_c\left(\frac{\theta_1}{2}\right), \tag{14}$$

$$A_p = R_c\left(\frac{\theta_1}{2}\right) P_1 R_c\left(\frac{\theta_2}{2}\right) M_c R_c\left(\frac{\theta_2}{2}\right) P_1 R_c\left(\frac{\theta_1}{2}\right), \tag{15}$$

$$A_s = R_c\left(\frac{\theta_1}{2}\right) P_1 R_c\left(\frac{\theta_2}{2}\right) M_c R_c\left(\frac{\theta_2}{2}\right) P_0 R_c\left(\frac{\theta_1}{2}\right) + R_c\left(\frac{\theta_1}{2}\right) P_0 R_c\left(\frac{\theta_2}{2}\right) M_c R_c\left(\frac{\theta_2}{2}\right) P_1 R_c\left(\frac{\theta_1}{2}\right) \tag{16}$$

with $M_c = e^{\gamma \sigma_z}$, $P_0 = |0\rangle\langle 0|$ and $P_1 = |1\rangle\langle 1|$. Following the standard approach of calculating the GBZ [19, 21], we write down the general eigenstate of U as

$$|\psi\rangle = \sum_{x,j} \beta_j^x |x\rangle \otimes |\phi_j\rangle_c, \tag{17}$$

where $|\phi_j\rangle_c$ is the coin state and β_j is the spatial-mode function. From the eigen equation $U|\psi\rangle = \lambda|\psi\rangle$, we obtain the bulk eigen equation

$$\left(A_m \beta + \frac{A_p}{\beta} + A_s - \lambda\right) |\phi\rangle_c = 0. \tag{18}$$

Eq. (18) supports nontrivial solutions only when

$$\det\left[A_m \beta + A_p \frac{1}{\beta} + A_s - \lambda\right] = 0, \tag{19}$$

which is a quadratic equation of β because $\det A_m = \det A_p = 0$. Explicitly, it reads

$$-\beta^2 \left(\cosh \gamma \cos \theta_1 \cos \theta_2 + \sinh \gamma \cos \theta_1\right) + \left(\lambda + \frac{1}{\lambda} + 2\cosh \gamma \sin \theta_1 \sin \theta_2\right) \beta + \sinh \gamma \cos \theta_1 - \cosh \gamma \cos \theta_1 \cos \theta_2$$

$$= 0. \tag{20}$$

Equation (20) has two solutions denoted as $\beta_1(\lambda)$ and $\beta_2(\lambda)$. In the thermodynamic limit, the open-boundary condition (OBC) requires that [19, 21]

$$|\beta_1(\lambda)| = |\beta_2(\lambda)|, \tag{21}$$

which is the GBZ equation. Combining it with quadratic Eq. (20), we have

$$|\beta_1| = |\beta_2| = \sqrt{\left|\frac{\cosh\gamma\cos\theta_2 - \sinh\gamma}{\cosh\gamma\cos\theta_2 + \sinh\gamma}\right|}. \tag{22}$$

Therefore, the GBZ is a circle with radius

$$|\beta| = \sqrt{\left|\frac{\cosh\gamma\cos\theta_2 - \sinh\gamma}{\cosh\gamma\cos\theta_2 + \sinh\gamma}\right|}. \tag{23}$$

This GBZ can be parameterized as $\beta = |\beta|e^{ip}$, with $p \in [0, 2\pi]$. For the left and right bulk (see the main article), $\theta_2 = \theta_2^L$ and θ_2^R, respectively. Note that θ_1 does not affect the GBZ.

η-pseudo-unitarity and non-Bloch exceptional points. In the exact PT phase, the Floquet operator must be pseudo-unitary, i.e., $\eta U^{-1}\eta^{-1} = U^\dagger$, with η being a Hermitian, invertible, linear operator [27, 28]. A key finding of our work is that, for non-Hermitian systems with non-Hermitian skin effect, the pseudo-unitarity of U is not in the BZ, but in the GBZ. In other words, we cannot find an η such that $\eta U^{-1}(k)\eta^{-1} \neq U^\dagger(k)$ with $k \in [0, 2\pi]$; however, such a symmetry can exist in the GBZ:

$$\eta U(\beta)^{-1}\eta^{-1} = U^\dagger(\beta)\big|_{\beta \in \text{GBZ}}. \tag{24}$$

Here, $U(\beta)$ is defined as the analytic continuation of the Bloch Floquet operator $U(k)$: $U(\beta) = U(k)|_{e^{ik} \to \beta}$. In the following, we first demonstrate the condition (in GBZ) for such a symmetry, and then extract the location of the non-Bloch exceptional points.

In our model, the Bloch Floquet operator in the BZ is

$$U(k) = \exp\left(-i\frac{\theta_1}{2}\sigma_y\right)\exp\left(i\frac{k}{2}\sigma_z\right)\exp\left(-i\frac{\theta_2}{2}\sigma_y\right)\exp\left(\sigma_z\gamma\right)\exp\left(-i\frac{\theta_2}{2}\sigma_y\right)\exp\left(i\frac{k}{2}\sigma_z\right)\exp\left(-i\frac{\theta_1}{2}\sigma_y\right), \tag{25}$$

which is obtained from the identifications $|x+1\rangle\langle x| \to e^{-ik}$, $|x-1\rangle\langle x| \to e^{ik}$ that lead to $S_1 \to e^{-ik\frac{1-\sigma_z}{2}}$ and $S_2 \to e^{ik\frac{1+\sigma_z}{2}}$.

To define the Floquet operator in the GBZ, we perform the replacement $e^{ik} \to \beta = |\beta|e^{ip}$

$$U(\beta) = \exp\left(-i\frac{\theta_1}{2}\sigma_y\right)\exp\left[\frac{i}{2}\left(p - i\ln|\beta|\right)\sigma_z\right]\exp\left(-i\frac{\theta_2}{2}\sigma_y\right)\exp\left(\sigma_z\gamma\right)\exp\left(-i\frac{\theta_2}{2}\sigma_y\right)$$
$$\times \exp\left[\frac{i}{2}\left(p - i\ln|\beta|\right)\sigma_z\right]\exp\left(-i\frac{\theta_1}{2}\sigma_y\right). \tag{26}$$

While $U(\beta)$ is a non-unitary 2×2 matrix, we can see that it still satisfies $\det U(\beta) = \det U^{-1}(\beta) = \det U^\dagger(\beta) = 1$ according to Eq. (26). Therefore, the additional condition needed for the pseudo-unitarity of $U(\beta)$ is $\text{Tr}[U^{-1}(\beta)] = \text{Tr}[U^\dagger(\beta)]$. These two conditions ensure that the product and sum of the two eigenvalues are the same for $U^{-1}(\beta)$ and $U^\dagger(\beta)$, therefore the eigenvalues should be the same, and there exists a certain η such that Eq. (24) holds. After a straightforward calculation, we obtain

$$\text{Tr}\left[U^{-1}(\beta) - U^\dagger(\beta)\right] = 2i\cos\theta_1\sin p\left[\frac{1}{|\beta|}(\sinh\gamma - \cosh\gamma\cos\theta_2) + |\beta|(\sinh\gamma + \cosh\gamma\cos\theta_2)\right]. \tag{27}$$

Inserting Eq. (23) into Eq. (27), we have

$$\text{Tr}[U^{-1}(\beta) - U^\dagger(\beta)] = 2i\cos\theta_1\sin p\left[-\sqrt{|uv|}\text{sgn}(u) + \sqrt{|uv|}\text{sgn}(v)\right], \tag{28}$$

where we have used the shorthand notations

$$u = \cosh\gamma\cos\theta_2 - \sinh\gamma, \quad v = \cosh\gamma\cos\theta_2 + \sinh\gamma. \tag{29}$$

It follows that

$$\text{Tr}[U^{-1}(\beta) - U^{\dagger}(\beta)] = \begin{cases} 0 & |\cos\theta_2| > |\tanh\gamma| \\ \pm 4i\cos\theta_1 \sin p\sqrt{|\cosh^2\gamma\cos^2\theta_2 - \sinh^2\gamma|} & |\cos\theta_2| < |\tanh\gamma| \end{cases}. \quad (30)$$

Therefore, we have shown that a necessary condition for $U(\beta)$ being pseudo-unitary is

$$|\cos\theta_2| > |\tanh\gamma|. \quad (31)$$

We have then numerically checked that the parameter region with $|\cos\theta_2| > |\tanh\gamma|$ coincides with the exact PT phase in the phase diagram Fig. 2d of the main text. Furthermore, we have checked that in the region with $|\cos\theta_2| > |\tanh\gamma|$, U actually satisfies the strong version of pseudo-unitary condition [28], namely that $\eta = \sum_n |\chi_n\rangle\langle\chi_n|$, where $|\chi_n\rangle$ is the nth left eigenstate of U, with $\langle\chi_n|U = \langle\chi_n|\lambda_n$ (λ_n is the nth eigenvalue of U) [28]. This condition is equivalent to that η can be decomposed as $\eta = OO^{\dagger}$ with O linear and invertible [28]. This strong pseudo-unitarity guarantees $|\lambda_n| = 1$ for all n, which translates to the complete reality of the quasienergy spectrum [28]. We have numerically checked that $\eta = \sum_n |\chi_n\rangle\langle\chi_n|$ indeed satisfies Eq. (24). Therefore, we are able to conclude that the non-Bloch exceptional points are given by the expression $|\cos\theta_2| = |\tanh\gamma|$.

Author contributions L.X. performed the experiments with contributions from K.W.; T.D., Z.W. and W.Y. performed the theoretical analysis; Z.W., W.Y. and P.X. initiated the project; P.X. supervised the experiment; all authors discussed the results; Z.W., W.Y. and P.X. wrote the paper with input from all authors. L.X. and T.D. contributed equally to this work.
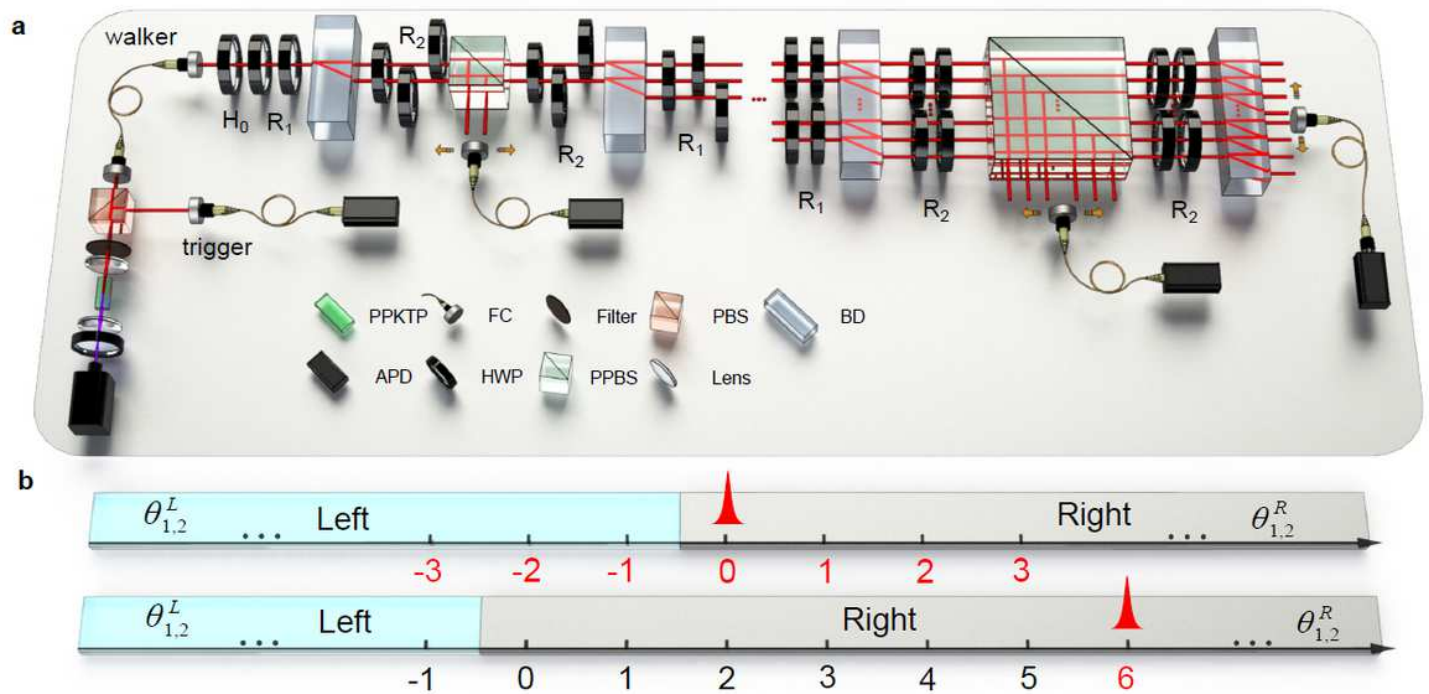
Additional information Correspondence and requests for materials should be addressed to Zhong Wang (wangzhongemail@tsinghua.edu.cn), Wei Yi (wyiz@ustc.edu.cn) and Peng Xue (email: gnep.eux@gmail.com).
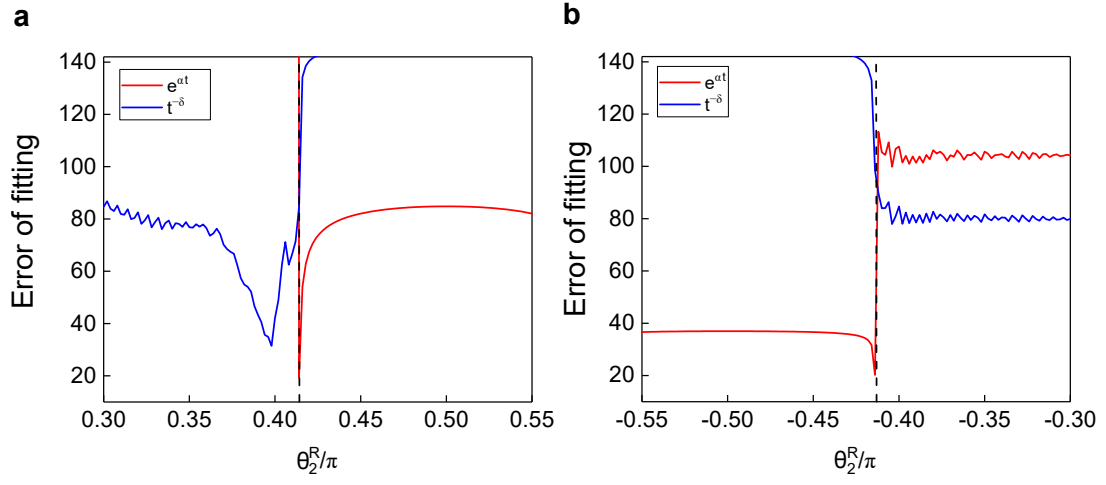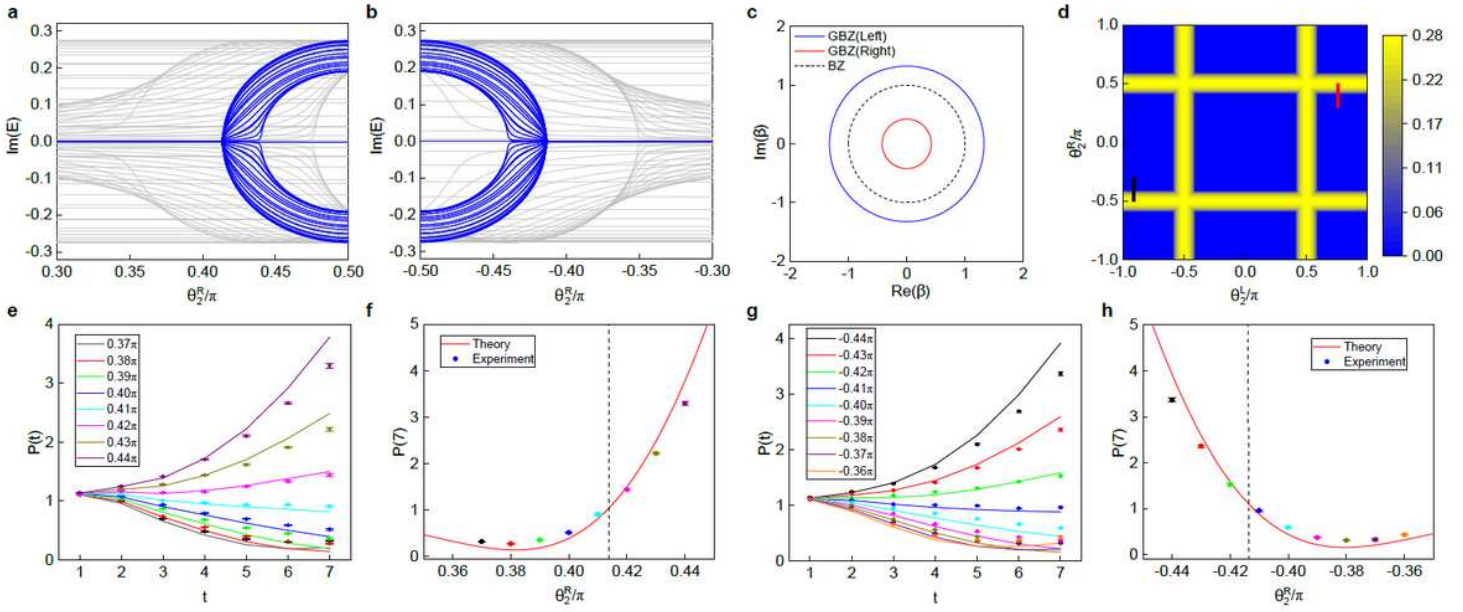
Extended Data Fig. 1. **Errors for fitting the corrected probability.** The accumulated variance $\sum_t [P_{x=6}(t) - f(t)]^2 / f^2(t)$ for an exponential fit (red) with $f(t) = e^{\alpha t}$; and a power-law fit (blue) with $f(t) = t^{-\delta}$. Here α and δ are fitting parameters. Parameters in **a** and **b** are the same as those in Figs. 3f and h, respectively.
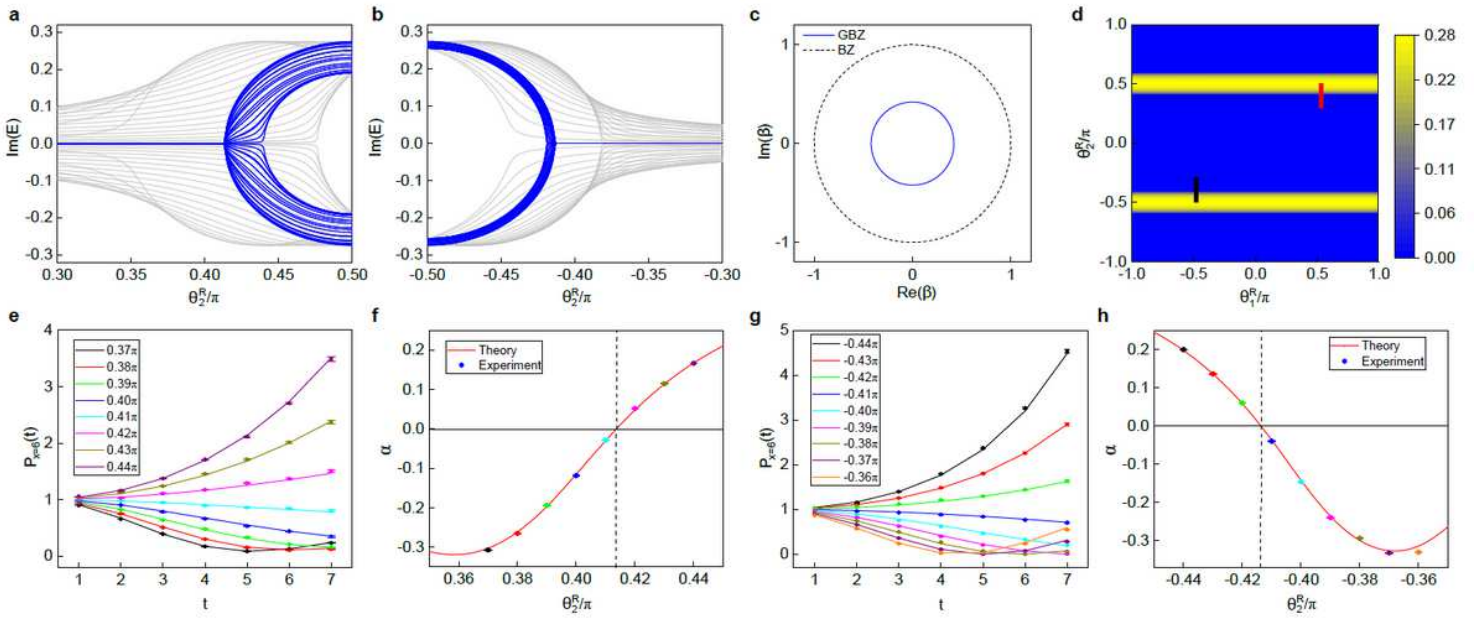
Figures

Figure 1

Experimental implementation. a, A pair of photons is generated via the spontaneous parametric down conversion in the periodically poled potassium titanyl phosphate crystal (PPKTP), with one serving as a trigger and the other (walker) projected into the quantum-walk network as the walker photon. After passing through a polarizing beam splitter (PBS) and a half-wave plate (HWP), the polarization of the walker photon is initialized as |0⟩. It then undergoes a quantum walk through an interferometric network, composed of HWPs, beam displacers (BDs), and partially polarizing beam splitter (PPBS), and is nally detected by avalanche photodiodes (APDs), in coincidence with the trigger photon. b, The domain-wall geometry of non-Hermitian quantum walks. Upper panel (Scheme I): the walker starts near the domain wall at x = 0. Lower panel (Scheme II): the walker starts from the bulk (i.e., far away from the domain wall) position x = 6.

Figure 2

Non-Bloch exceptional points from domain-wall measurements. a, b, Imaginary part of quasienergies, Im(E) versus θ_{R2}. Other coin parameters are fixed at θ_{R1} = 0.5625π and θ_{L1} = −0.0625π. We take θ_{L2} = 0.75π and −0.9735π for a and b, respectively. Blue and gray lines represent the OBC (non-Bloch) and PBC (Bloch) spectra, respectively. The blue non-Bloch spectra feature an exceptional point at $|\theta_{R2}|$ = 0.413π, while the gray Bloch spectra remain complex-valued throughout. c, Brillouin zone and GBZ for θ_{R1} = 0.5625π, θ_{L1} = −0.0625π, θ_{R2} = −0.44π and θ_{L2} = −0.9375π. d, Numerically calculated max[Im(E)] for θ_{R1} = 0.5625π and θ_{L1} = −0.0625π. The yellow (blue) region is the broken (exact) PT phase. The red and black cuts correspond to a, e, f and b, g, h, respectively. e, Experimentally measured P(t) (symbols) with an initial state $|\psi(t = 0)\rangle = |0\rangle_x \otimes |0\rangle_{coin}$ up to seven steps for eight different values of θ_{R2}, together with the theoretical predictions (curves). Other coin parameters are the same as in a, e.g., θ_{L2} = 0.75π. f, P(t = 7) under the same parameters as those in c. Error bars indicate the statistical uncertainty obtained by assuming Poissonian statistics. g, h, The same as e, f except that θ_{L2} = −0.9735π. The loss parameter is fixed at γ = 0.2746 throughout our experiment.

Figure 3

Non-Bloch exceptional points from bulk measurements. a, Im(E) versus θR2 , with θR1 = 0.5625π fixed. b, Im(E) versus θR2 , with θR1 = −0.4688π fixed. c, GBZ of the right region, for θR1 = −0.4688π and θR2 = −0.44π. d, Numerically calculated max[Im(E)]. The blue and yellow regions correspond to the exact and broken PT phase, respectively. e, Experimentally measured Px=6(t) (symbols) with an initial state |ψ(0)i = |6ix ⊗ |0icoin for eight values of θR2 , compared to the theoretical predictions (curves). Here we fix θR1 = 0.5625π. f, Exponent α versus θR2 extracted from the data in e. The red line is plotted from numerical simulations of 7-step evolutions. g, h The same as c, d, except that θR2 = −0.5π. e, f and g, h correspond to the red and black cuts in the phase diagram d, respectively. The left region is idle throughout measurements, which are performed in the right region only. Without loss of generality, we take θL1 = −0.0625π and θL2 = 0.75π for a, b, and θL1 = −0.0625π and θL2 = −0.9375π for g, h.